2021

IP3R-driven increases in mitochondrial Ca2+ promote neuronal death in NPC disease

Scott A. Tiscione

Maria Casas

Jonathan D. Horvath

Vincent Lam

Keiko Hino

See next page for additional authors

Authors

Scott A. Tiscione, Maria Casas, Jonathan D. Horvath, Vincent Lam, Keiko Hino, Daniel S. Ory, L. Fernando Santana, Sergi Simó, Rose E. Dixon, and Eamonn J. Dickson

IP_3R-driven increases in mitochondrial Ca^{2+} promote neuronal death in NPC disease

Scott A. Tiscione[a], Maria Casas[a], Jonathan D. Horvath[a], Vincent Lam[a], Keiko Hino[b], Daniel S. Ory[c], L. Fernando Santana[a], Sergi Simó[b], Rose E. Dixon[a], and Eamonn J. Dickson[a,1]

[a]Department of Physiology and Membrane Biology, University of California, Davis, CA 95616; [b]Department of Cell Biology and Human Anatomy, University of California, Davis, CA 95616; and [c]Department of Internal Medicine, Washington University School of Medicine, St. Louis, MO 63110

Edited by Mark T. Nelson, University of Vermont, Burlington, VT, and approved July 31, 2021 (received for review June 9, 2021)

Ca^{2+} is the most ubiquitous second messenger in neurons whose spatial and temporal elevations are tightly controlled to initiate and orchestrate diverse intracellular signaling cascades. Numerous neuropathologies result from mutations or alterations in Ca^{2+} handling proteins; thus, elucidating molecular pathways that shape Ca^{2+} signaling is imperative. Here, we report that loss-of-function, knockout, or neurodegenerative disease–causing mutations in the lysosomal cholesterol transporter, Niemann-Pick Type C1 (NPC1), initiate a damaging signaling cascade that alters the expression and nanoscale distribution of IP_3R type 1 (IP_3R1) in endoplasmic reticulum membranes. These alterations detrimentally increase G_q-protein coupled receptor–stimulated Ca^{2+} release and spontaneous IP_3R1 Ca^{2+} activity, leading to mitochondrial Ca^{2+} cytotoxicity. Mechanistically, we find that SREBP-dependent increases in Presenilin 1 (PS1) underlie functional and expressional changes in IP_3R1. Accordingly, expression of PS1 mutants recapitulate, while PS1 knockout abrogates Ca^{2+} phenotypes. These data present a signaling axis that links the NPC1 lysosomal cholesterol transporter to the damaging redistribution and activity of IP_3R1 that precipitates cell death in NPC1 disease and suggests that NPC1 is a nanostructural disease.

calcium | IP_3R | NPC1 | neurodegeneration | GPCR

Calcium (Ca^{2+}) is the most-ubiquitous second messenger in neurons. For this reason, spatial and temporal elevations in cytosolic Ca^{2+} signals are tightly controlled, with elevations in cytoplasmic Ca^{2+} used to initiate and orchestrate a host of diverse intracellular signaling cascades fundamentally required for neuronal development, synaptic plasticity, neurotransmission, and neuron fidelity (for review, refer to refs. 1, 2). One of the primary mechanisms to elevate intracellular Ca^{2+} levels is through release of Ca^{2+} from the largest intracellular Ca^{2+} store, the endoplasmic reticulum (ER). Ca^{2+} can be rapidly mobilized from the ER into the cytoplasm through the Inositol 1,4,5-triphosphate receptor (IP_3R), a ligand-gated Ca^{2+} channel in the ER membrane. IP_3Rs are activated when cell surface G_q-protein coupled receptors (G_qPCR) stimulate phospholipase C (PLC) to hydrolyze the plasma membrane (PM) lipid $PI(4,5)P_2$ into soluble IP_3, the native agonist of the IP_3Rs (3). IP_3Rs are further regulated by phosphorylation, protein–protein interactions, and local Ca^{2+} concentrations (3, 4).

Niemann-Pick Type C1 (NPC1) disease is an autosomal recessive lysosomal storage disorder that arises from mutations in the gene encoding the lysosomal NPC1 protein. This transmembrane cholesterol transporter facilitates the egress of cholesterol from the acidic compartment to other cellular membranes with its loss-of-function resulting in the cellular hallmark of NPC1 disease: an accumulation of lipids within the lysosome and perturbations in cellular cholesterol homeostasis. The underlying mechanisms linking cholesterol dysregulation and lipid accumulation to neurodegeneration are not well understood; however, impaired Ca^{2+} signaling is a consequence of NPC1 disease mutations (5–7). Given that dysfunctional Ca^{2+} signaling is a common feature in neurodegenerative disease and is thought to precede and contribute to neuronal cell death (2, 8), understanding the link between NPC1 function and intracellular Ca^{2+} becomes imperative.

There are three IP_3R isoforms: IP_3R Type 1 (IP_3R1), Type 2, and Type 3, each with its own differential expression across cell types and tissues. IP_3R1 protein is most abundantly expressed in soma and synaptic regions of the brain, including Purkinje cells of the cerebellum (9), the most impacted cell type in NPC1 disease (10). Functionally, IP_3R1 is essential for a variety of intracellular events including G_qPCR signaling (11), synaptic strengthening (12), Ca^{2+}-dependent gene transcription (11), and Ca^{2+} transfer at ER–mitochondrial membrane contact sites (MCS) (13). Behaviorally, $IP_3R1^{-/-}$ mice die in utero or only live for a few weeks while exhibiting severe neurological symptoms such as ataxia and seizures (14), while specific cerebellum loss (15) or disease mutations in the IP_3R1 gene lead to ataxias (16, 17) and Gillespie syndrome (18). Given IP_3R1's importance in neurological function and development, and our previous reports of decreased $PI(4,5)P_2$ levels (precursor of IP_3) as well as reductions in ER Ca^{2+} (source of G_qPCR Ca^{2+}) in multiple models of NPC disease (19, 20), we hypothesized that IP_3R signaling may be perturbed in NPC1 disease.

Using a combination of murine and patient disease models of NPC1 disease, we show that despite reduced $PI(4,5)P_2$ (19) and ER Ca^{2+} (20), IP_3-mediated Ca^{2+} release is paradoxically increased. We determine that loss of NPC1 function results in larger and more numerous immobile IP_3Rs clusters near the PM that drive spontaneous Ca^{2+} release events (Ca^{2+} puffs) and prime IP_3R to release more Ca^{2+} during G_qPCR activation. The cellular consequences of enhanced IP_3R clustering and activity are 1) decreased ER Ca^{2+} levels, 2) increased nuclear factor of activated T-cells (NFAT) signaling, and 3) increased mitochondrial

Significance

NPC1 is a ubiquitously expressed lysosomal cholesterol transporter whose loss of function results in neurodegenerative NPC1 disease. Here, we report that loss-of-function, knockout, or mutation-causing NPC1 initiates a damaging signaling cascade that alters the expression and nanoscale distribution of IP_3R type 1 that precipitates neuron death. Targeting IP_3R1 or upstream elements of this signaling cascade rescues neuronal death and provides potential therapeutic targets to address IP_3R dysfunction, a feature of NPC1 disease and other neurodegenerative disorders.

Author contributions: S.A.T., M.C., R.E.D., and E.J.D. designed research; S.A.T., M.C., J.D.H., V.L., K.H., S.S., and E.J.D. performed research; D.S.O. and L.F.S. contributed new reagents/analytic tools; S.A.T., M.C., J.D.H., V.L., K.H., S.S., R.E.D., and E.J.D. analyzed data; and S.A.T., M.C., J.D.H., D.S.O., L.F.S., S.S., R.E.D., and E.J.D. wrote the paper.

The authors declare no competing interest.

This article is a PNAS Direct Submission.

[1]To whom correspondence may be addressed. Email: ejdickson@ucdavis.edu.

This article contains supporting information online at https://www.pnas.org/lookup/suppl/doi:10.1073/pnas.2110629118/-/DCSupplemental.

Published September 27, 2021.

Ca^{2+}, which leads to neuronal Ca^{2+} cytotoxicity. We propose that the lysosomal NPC1 cholesterol transporter can tune the distribution and activity of IP_3R in health, while its loss of function, such as in NPC1 disease, initiates a pervasive signaling cascade that triggers mitochondrial cytotoxicity.

Results

Loss of NPC1 Function Potentiates G_q-Mediated Ca^{2+} Signaling. We have previously reported that both ER-Ca^{2+} stores and PM PI(4,5)P_2 levels are significantly reduced in NPC1 disease (19, 20). Given that IP_3R-mediated Ca^{2+} release requires both a steep Ca^{2+} gradient across the ER and IP_3's precursor, PI(4,5)P_2, (Fig. 1*A*), we tested the hypothesis that cytosolic Ca^{2+} signals evoked from IP_3Rs following activation of a G_qPCR were perturbed in NPC1 loss-of-function cells. First, we compared G_qPCR responses from control and U18666A-treated (U18; specific inhibitor of NPC1) (21) tsA201 cells loaded with the cytosolic Ca^{2+} indicator Fluo-4 and treated with histamine, an agonist for the G_q-coupled histamine H_1 receptor, in a Ca^{2+}-free solution to eliminate extracellular Ca^{2+} contribution. Analysis of the resulting Ca^{2+} responses revealed that overnight inhibition of NPC1 significantly increased the amount of Ca^{2+} released into the cytoplasm (Fig. 1 *B* and *C*). Similar results were observed from NPC1$^{-/-}$ cells (Fig. 1 *D* and *E*) and patient fibroblasts harboring the most prevalent patient mutation (NPC1^{I1061T}; Fig. 1 *F* and *G*). To confirm that NPC1-dependent increases in G_qPCR-mediated Ca^{2+} release were conserved in neurons, we performed similar experiments in two murine models of NPC1 disease: 1) NPC1 knockout (NPC1$^{-/-}$) neurons and 2) Npc1$^{tm(I1061T)Dso}$ (hereafter referred to as NPC1^{I1061T}) neurons, which recapitulate the pathological features of the most prevalent human disease allele (22). Similar to cell models, both NPC1$^{-/-}$ (Fig. 1 *H* and *I*) and NPC1^{I1061T} (Fig. 1 *J* and *K*) neurons exhibited significantly larger elevations in Ca^{2+} following G_qPCR stimulation as compared to wild type (WT) control neurons. Thus, across all models of NPC1 disease, including primary neurons, IP_3R-mediated Ca^{2+} release was significantly increased.

NPC1 Inhibition or Disease Mutation Alters IP_3R1 Expression and Distribution. To determine the molecular mechanism(s) underlying increased G_qPCR-induced Ca^{2+} release, we first measured mRNA levels from each of the PM elements along the G_qPCR signaling cascade from receptors to PLC enzymes (*SI Appendix*, Fig. S1 *A* and *B*). Quantification of gene transcripts from control and NPC1^{I1061T} patient cells revealed that several varieties of receptor, $G\alpha_q$, and PLC isoforms were unaltered following loss of NPC1 function. The sole exception was PLCβ2, which had elevated messenger ribonucleic acid (mRNA) levels (*SI Appendix*, Fig. S1*B*) but unaltered protein levels (*SI Appendix*, Fig. S1*C*) in NPC1^{I1061T} cells relative to control. Based on these analyses, the observation that three different G_qPCR agonists (histamine, purinergic, and muscarinic) all resulted in enhanced Ca^{2+} release (Fig. 1 *B*–*K*), and our previous determination that PM PI(4,5)P_2 is decreased in NPC1 disease (19) suggest that the molecular element(s) responsible for enhancing G_qPCR signaling in NPC1 disease cells do not lie at the PM.

We next examined whether elements downstream of PI(4,5)P_2 are involved in potentiating G_qPCR Ca^{2+} release in NPC1 cells. To begin, we analyzed IP_3R1, as it is 1) the most common isoform in the brain and 2) abundantly expressed in Purkinje cells of the cerebellum (9), the most vulnerable neuronal cell type in NPC (23). Western blot analysis determined that NPC1^{I1061T} patient cells had a 2.6-fold increase in protein levels compared to control (Fig. 2*A*). To test whether this expressional change in IP_3R1 protein levels translates to a functional role in potentiating G_qPCR Ca^{2+} release, we treated IP_3R1 knockout ($IP_3R1^{-/-}$) human embryonic

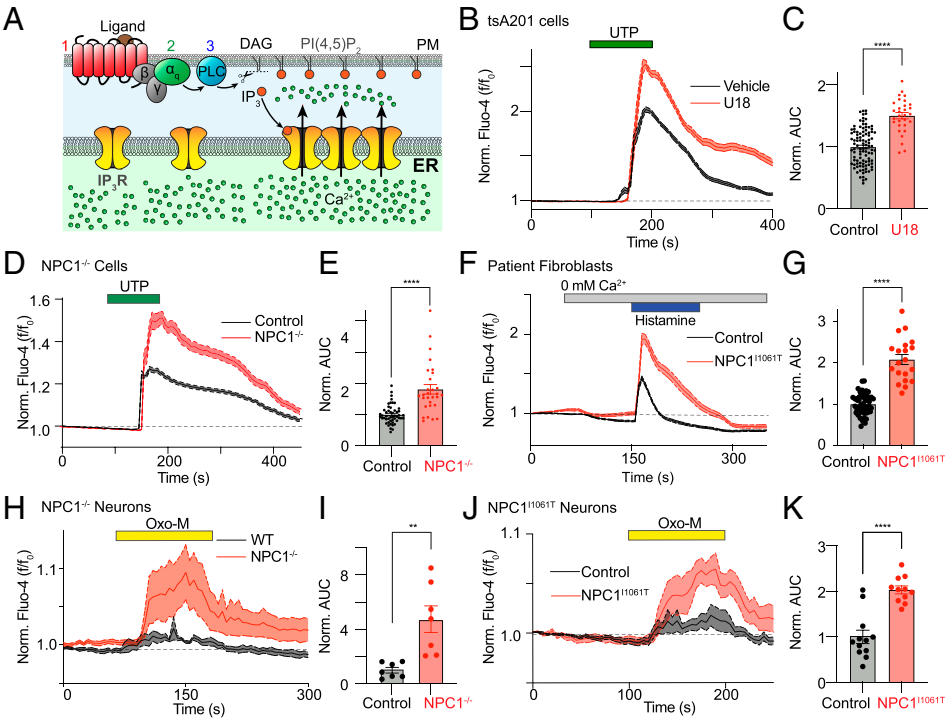

Fig. 1. G_qPCR Ca^{2+} release is enhanced in NPC1 disease. (*A*) G_qPCR signaling pathway. (*B*) Average time series of Fluo-4 loaded control (black) and U18-treated (red) tsA201 cells treated with UTP (100 μM). (*C*) Quantitative analysis of the UTP-evoked Ca^{2+} area under the curve (AUC). (*D* and *E*) Same as *B* and *C*, only NPC1$^{-/-}$ cells. (*F* and *G*) Same as *B* and *C*, only control and NPC1^{I1061T} patient cells and treated with histamine (100 μM). (*H* and *I*) Same as *B* and *C*, only NPC1$^{-/-}$ neurons treated with Oxo-M. (*J* and *K*). Same as *B* and *C*, only NPC1^{I1061T} neurons treated Oxo-M. All the data are expressed as mean ± SEM from individual cells. Statistical analysis was an unpaired *t* test. ***$P < 0.001$; ****$P < 0.0001$.

kidney 293 (HEK) cells with U18 and evoked IP_3R-mediated Ca^{2+} release using the purinergic receptor agonist, UTP (100 μM) (24). Unlike overnight U18 treatment in control cells (Fig. 1*B*), we found that incubating $IP_3R1^{-/-}$ cells with U18 did not alter G_qPCR Ca^{2+} responses (Fig. 2 *B* and *C*). These data support a model wherein increased IP_3R1 protein levels facilitate augmented IP_3R-mediated signaling following NPC1 dysfunction.

The spatial distribution of IP_3Rs influences ER Ca^{2+} release, inactivation, wave propagation, and oscillations (3, 25–27). To determine whether increased protein levels alter the spatial organization of IP_3R1, we took several complementary fluorescent approaches to visualize the endogenous distribution of IP_3R1 in isolated cells, including neurons, and intact brain slices. To begin, we used HeLa cells with endogenous IP_3R1 tagged with a monomeric eGFP (eGFP-IP_3R cells) (28). eGFP-IP_3R cells allow us to quantify the endogenous distribution of the IP_3R1 without influence from overexpression or off-target binding of immunofluorescent antibodies. Total internal reflection fluorescence (TIRF) microscopy, to visualize IP_3R1 close to the PM, revealed that U18 treatment increased both the area and number of IP_3R1 clusters close to the PM (Fig. 2 *D* and *E*). To independently confirm that loss of NPC1 function alters IP_3R1 distribution near the PM, we performed immunofluorescence experiments on patient fibroblasts, neurons, and brain slices from the $NPC1^{I1061T}$ murine model using a validated IP_3R1 antibody (*SI Appendix*, Fig. S2 *A–D*). TIRF imaging from patient fibroblasts determined that NPC1 disease mutations also increase IP_3R1 cluster size and number (Fig. 2 *F* and *G*). Similarly, IP_3R1 cluster intensity and area was increased at both the soma and neurites of isolated hippocampal (Fig. 2 *H* and *I*) and cortical neurons (Fig. 2 *J* and *K*). Finally, to ensure that 1) IP_3R1 clustering occurs in intact brain regions and 2) increased IP_3R1 cluster size occurs in brain regions affected by NPC1 disease, cerebellar slices from age-matched wild-type and symptomatic $NPC1^{I1061T}$ animals were fixed and double immunostained for IP_3R1 and the Purkinje cell marker calbindin. In agreement with our single-cell data, IP_3R1 clusters within the Purkinje cell soma was significantly larger in NPC1 disease cerebellar sections than controls (Fig. 2*L*). Collectively, these data present strong evidence that loss of NPC1 function increases expression and distribution of IP_3R1 to enhance cluster size and increase G_qPCR-mediated Ca^{2+} release.

Nanoscale Distribution of IP_3R1 Is Altered in NPC1 Disease. Having demonstrated that IP_3R1 clustering and distribution is altered near the PM in NPC1 disease using diffraction-limited approaches, we next wanted to precisely map and quantify the nanoscale organization of IP_3R1 at the PM using superresolution single-molecule localization microscopy in TIRF mode ($superresolution_{TIRF}$; resolution is approximately 20 nm) (29). This is important, because it allows us to investigate the nanoscale molecular architecture within and between IP_3R1 clusters to determine whether they are altered in NPC1 disease cells.

Quantitative analysis of $superresolution_{TIRF}$ localization maps from control and U18-treated eGFP-IP_3R cells revealed that similar to diffraction-limited images, NPC1 inhibition resulted in an increase in both IP_3R cluster size and density (Fig. 3 *A* and *B*). Similar results were also obtained from neurons (Fig. 3 *C* and *D*). During analysis of localization maps, we noticed that single IP_3R1 clusters visualized using conventional TIRF microscopy actually consisted of many discrete puncta when imaged with superresolution microscopy (*SI Appendix*, Fig. S3 *A–E*). Cells lacking NPC1 function displayed a higher density of puncta in these discrete localized areas (*SI Appendix*, Fig. S3 *D–F*). Further, nearest-neighbor analysis measuring the distance from both a centroid and perimeter (*SI Appendix*, Fig. S3*C*) of these discrete puncta indicated that puncta were more closely associated with one another in U18-treated cells (*SI Appendix*, Fig. S3 *G–J*). Together, these data present evidence that loss of NPC1 function not only increases IP_3R puncta size but also increases the density of IP_3R1 puncta both within and between a cluster in NPC1 disease.

IP_3R1 Cluster Mobility and Activity Are Increased in NPC1 Disease. Given that IP_3R1 cluster size is increased in NPC1 disease, we wanted to determine whether the mobility of IP_3R1 in the ER was altered. To this end, we used fluorescent recovery after photobleaching to quantify the mobility of eGFP-tagged IP_3R1 clusters both near the PM (*SI Appendix*, Fig. S4 *A–C*) and within the cell interior (*SI Appendix*, Fig. S4 *D–F*). Fitting of fluorescence recovery kinetics after photobleaching revealed that the mobile fraction of IP_3R1 in U18- treated eGFP-IP_3R cells was significantly reduced compared to vehicle controls both near the PM (*SI Appendix*, Fig. S4*C*) and near the middle of the cell (*SI Appendix*, Fig. S4*F*).

Recently, it has been reported that immobile IP_3R1 clusters localized close to ER–PM junctions are optimally positioned to respond to receptor-generated IP_3 to initiate Ca^{2+} signals (28). Further, immobile IP_3R clusters have been observed to be the site of spontaneous localized Ca^{2+} release from the ER, termed "Ca^{2+} puffs" (28), with the activity of puffs further influenced by the number of IP_3R within the originating cluster (25, 30). Given that IP_3R1 clusters are larger, contain more discreet IP_3R1 puncta within a cluster, and are more immobile following NPC1 dysfunction, we wanted to determine whether spontaneous Ca^{2+} puffs were altered. First, we loaded eGFP-IP_3R cells with the Ca^{2+} dye Calbryte590 and simultaneously measured IP_3R1 distribution and spontaneous Ca^{2+} activity. This approach allows us to measure and correlate Ca^{2+} activity in the same region as IP_3R1 (Fig. 4*A*). We define this signal simply as $Ca^{2+}{}_{IP3R1}$, because 1) the Ca^{2+} signal originates within the same location as IP_3R1, 2) is sensitive to the IP_3R antagonist Xestospongin C (*SI Appendix*, Fig. S5 *A* and *C*), and 3) spontaneous Ca^{2+} signals occur in the absence of extracellular Ca^{2+} (*SI Appendix*, Fig. S5*B*). We do acknowledge the possibility that these Ca^{2+} signals may not only result from IP_3R1 but represent a convolved signal from other Ca^{2+} sources. That being said, analysis of spontaneous $Ca^{2+}{}_{IP3R1}$ signals determined that the amplitude, duration, and number of spontaneous Ca^{2+} events were all significantly elevated in U18-treated cells relative to control (Fig. 4 *B* and *C*), consisted with previous reports of increased spontaneous activity with larger IP_3R clusters.

To test whether disease mutations exhibit altered $Ca^{2+}{}_{IP3R1}$, we loaded control and $NPC1^{I1061T}$ patient fibroblasts with Fluo-4 and measured spontaneous Ca^{2+} activity. Similar to U18-treated cells, $NPC1^{I1061T}$ cells also had increased amplitude, duration, and mass (volume) of Ca^{2+} puffs compared to healthy controls (Fig. 4 *D–I*). To further investigate a role for IP_3R1 in facilitating these increases in Ca^{2+} activity, we treated control and $IP_3R1^{-/-}$ cells with U18 or vehicle control and quantified spontaneous Ca^{2+} events. We found that treatment with U18 recapitulated the Ca^{2+} puff phenotype observed in eGFP-IP_3R cells and $NPC1^{I1061T}$ fibroblasts, while $IP_3R1^{-/-}$ cells were insensitive to the U18 (Fig. 4 *J* and *K*). Peak fluorescence of Ca^{2+} puffs was also quantified showing no significant difference between vehicle and U18 treatment in both cell types but a significant reduction in $IP_3R1^{-/-}$ cells (Fig. 4*L*). These results indicate that the altered nanoscale distribution of IP_3R1 contribute to enhanced Ca^{2+} puff activity in NPC1 disease.

Presenilin 1 Alters IP_3R1 Distribution and Function in NPC1 Disease. Having established that G_qPCR-mediated Ca^{2+} signaling, IP_3R1 distribution, and IP_3R1 activity are all severely altered in NPC1 disease, we next wanted to identify the underlying mechanism(s) responsible for these changes. Recently, we have reported that increases in full-length, holoprotein, Presenilin 1 (PS1) expression is involved in mediating decreases in ER Ca^{2+} in NPC1 disease (20). Further, Alzheimer's disease mutations in PS1 ($PS1^{D257A}$) that shift expression mostly to the holoprotein form have previously been

NEUROSCIENCE

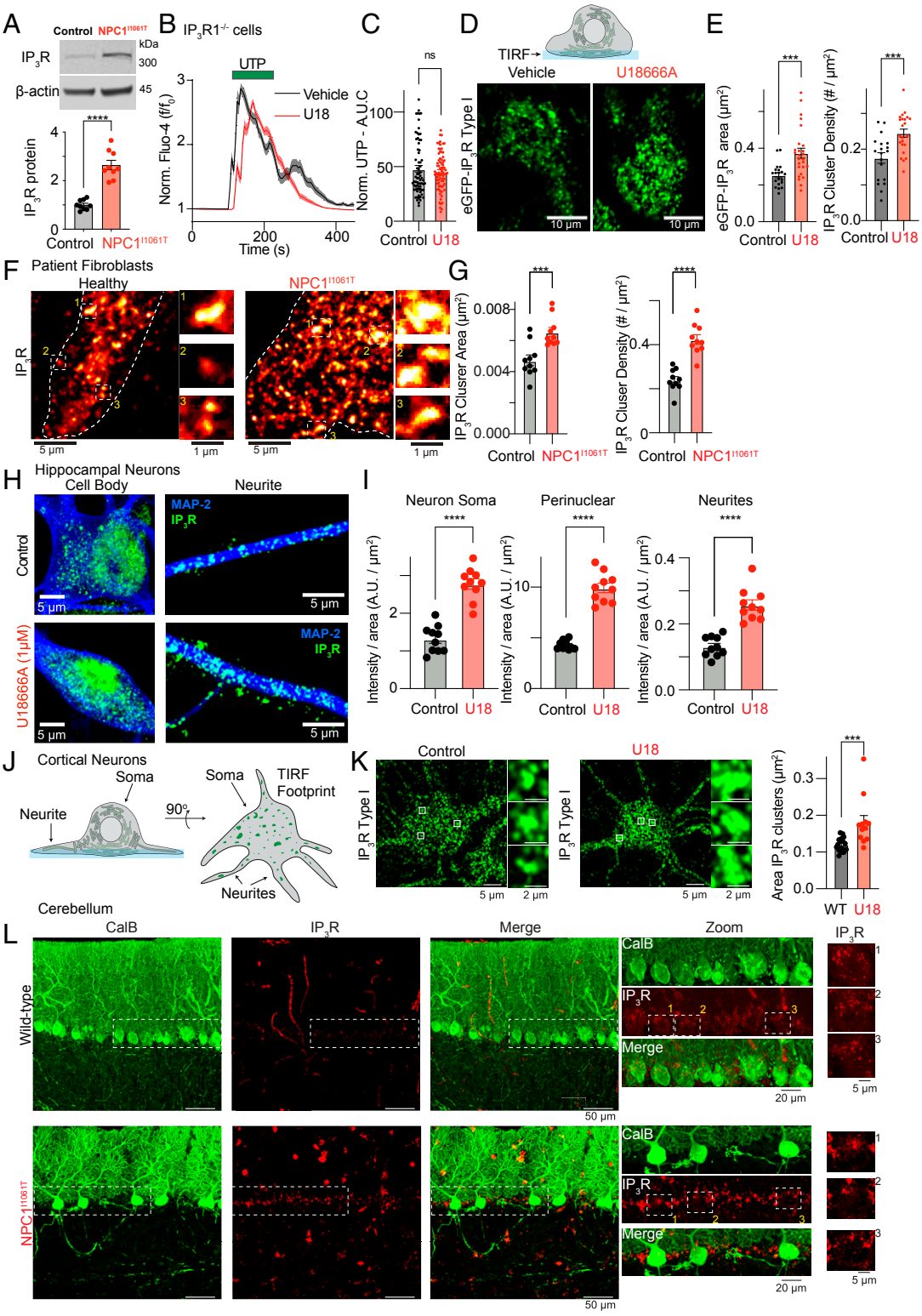

Fig. 2. IP_3R1 expression and distribution is remodeled in NPC1 disease. (*A*, *Top*) representative Western blot of IP_3R1 in control and $NPC1^{I1061T}$ disease fibroblasts. (*Bottom*) Quantification of IP_3R1 protein expression, normalized to β-Actin. (*B*) Average time series of Fluo-4 loaded control (black) and $IP_3R1^{-/-}$ (red) HEK cells, treated with UTP. (*C*) Quantitative analysis of the UTP-evoked Ca^{2+} area under the curve (AUC). (*D*, *Top*) Schematic of TIRF imaging. (*Bottom*) Representative TIRF images from eGFP-IP_3R HeLa cells, treated with vehicle (*Left*) or U18 (*Right*). (*E*, *Left*) Quantification of average IP_3R puncta area. (*Right*) IP_3R density. (*F*) Representative TIRF images from control (*Left*) and $NPC1^{I1061T}$ (*Right*) patient fibroblasts fixed and stained for IP_3R1. (*G*) Quantification of IP_3R1 cluster area (*Left*) and density (*Right*) from patient fibroblasts. (*H*) Representative images from cell body (*Left*) and neurite (*Right*) regions of control (*Top*) and U18-treated (*Bottom*) hippocampal neurons fixed and stained for IP_3R1 and MAP2. (*I*) Quantification of IP_3R1 intensity. (*J*) Schematic of TIRF image in neuron. (*K*) Representative images from control (*Left*) and U18-treated (*Right*) cortical neurons fixed and stained for IP_3R1. Insets show zoomed regions containing IP_3R1 clusters. (*Right*) Quantification of IP_3R1 cluster area. (*L*) Representative cerebellar sections from wild-type (*Top*) and $NPC1^{I1061T}$ brains fixed and stained for calbindin and IP_3R1. All the data are expressed as mean ± SEM from individual cells. Statistical analyses were unpaired *t* tests. ns: not significant; ***$P < 0.001$; ****$P < 0.0001$.

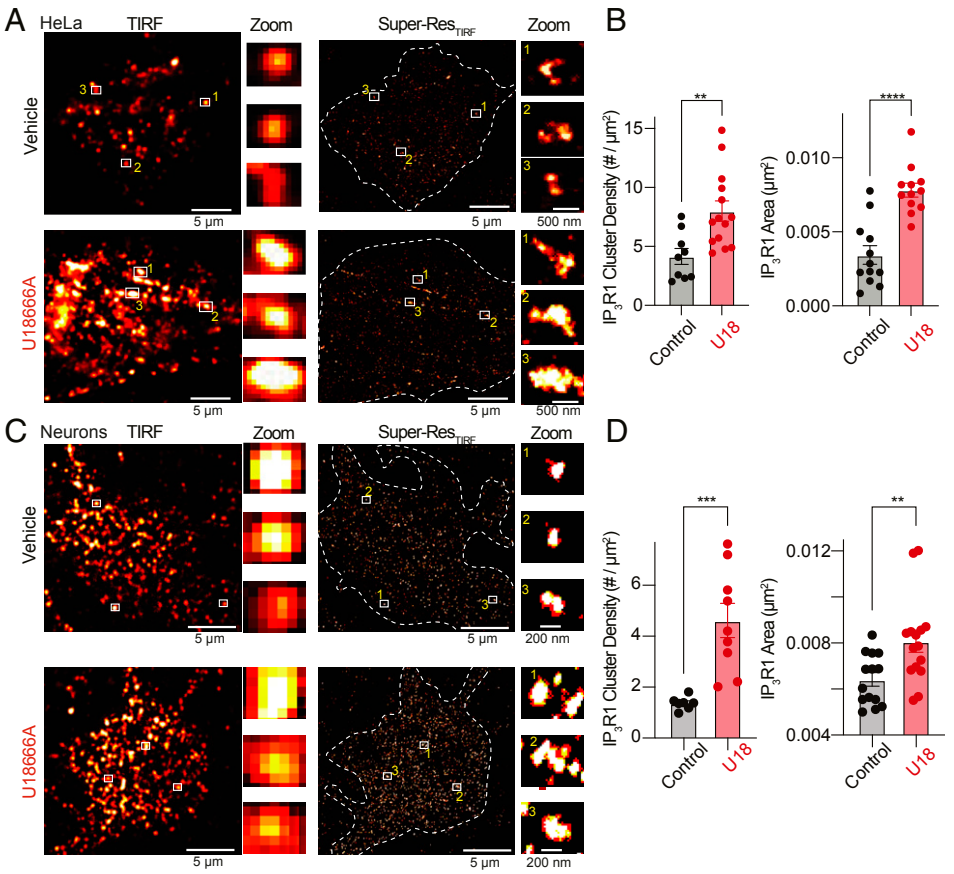

Fig. 3. Nanoscale distribution of IP_3R1 is remodeled in NPC1 disease. (*A*, *Left*) Representative TIRF images of Vehicle (*Top*) and U18-treated (*Bottom*) eGFP-IP_3R HeLa cells fixed and immunostained with an anti-GFP antibody. (*Right*) Superresolution localization map from the same cell. Zoomed regions are from white solid rectangles. (*B*) Quantification of density and area of eGFP-IP_3R1. (*C* and *D*) Same as *A* and *B*, only cortical neurons fixed and stained for IP_3R1. All the data are expressed as mean ± SEM from individual cells. Statistical analyses were unpaired *t* tests. $*P < 0.05$; $**P < 0.01$; $***P < 0.001$; $****P < 0.0001$.

reported to interact and produce exaggerated gain of function alterations to the biophysical gating properties of IP_3Rs (31, 32). To interrogate a role for PS1 in tuning IP_3R1 distribution/function, we first transfected HeLa cells with HA-PS1 (HA-PS1-WT) or HA-tagged $PS1^{D257A}$ and treated overnight with either vehicle control or U18 (10 µM; Fig. 5 *A* and *B*). TIRF imaging revealed that PS1-WT formed discrete clusters close to the PM, with cluster area significantly increased following overnight treatment with U18 to inhibit NPC1 function (Fig. 5 *A* and *B*). Interestingly, the $PS1^{D257A}$ mutation also clustered close to the PM and displayed a similar mean cluster size as the PS1-WT group treated with U18 (Fig. 5 *A* and *B*). Treatment of $PS1^{D257A}$-expressing cells with U18 did not further increase PS1 cluster area (Fig. 5*B*). These data suggest that loss of NPC1 function or Alzheimer's disease mutations increase the size of PS1 clusters near the PM. To test whether these increases correlate with changes in IP_3R1 distribution, we expressed the aforementioned constructs in eGFP-IP_3R1 HeLa cells and calculated Pearson's correlation coefficients. Image analysis revealed that U18 treatment significantly increases the colocalization of PS1 to IP_3R1 (compare Fig. 5 *C* and *D*), while the $PS1^{D257A}$ mutant also colocalizes more with IP_3R compared to wild-type PS1 even in the absence of NPC1 inhibition (Fig. 5*E*; analysis in Fig. 5*F*). These data are consistent with published observations that PS1 physically interacts with IP_3R1 and suggests there is a strong correlation between PS1 cluster size and IP_3R1 distribution. To test whether the full-length form of PS1, which is increased in NPC1 disease (20), alters IP_3R1, we overexpressed $PS1^{D257A}$ in eGFP-IP_3R1 HeLa cells. Aligned with a key role for the holoprotein in mediating the distribution/function of IP_3R1, expression of $PS1^{D257A}$ increased both IP_3R1 clusters (Fig. 5 *G* and *H*) and G_qPCR-mediated Ca^{2+} release (Fig. 5 *I* and *J*) to a similar extent as disease mutations or inhibition of NPC1. Altogether, these results suggest that enhanced PS1 cluster size may be responsible for altered nanoscale distribution/function of IP_3R1 following NPC1 loss of function.

A key question remained whether Ca^{2+} potentially coming through PS1 (33) can contribute to increases in IP_3R1, or whether only physical interactions (31) between the two proteins are important. To begin answering this question, we treated eGFP-IP_3R1 cells with the Sacro/ER Ca^{2+}-ATPase (SERCA) inhibitor Thapsigargin or the Ca^{2+} chelating agent EGTA in a 0-mM, Ca^{2+}-containing extracellular solution (*SI Appendix*, Fig. S6 *A–D*) and quantified IP_3R1 clusters near the PM over a period of 60 mins. Under each of these cytoplasmic Ca^{2+}-altering conditions, IP_3R1 cluster size significantly decreased near the PM, independently of alterations in the cell footprint (*SI Appendix*, Fig. S6 *E–M*). Thus, although modulating cytoplasmic Ca^{2+} concentrations does alter IP_3R1 clustering near the PM, it is in the opposing direction compared to loss of NPC1 function.

Next, to test a direct role for PS1 driving IP_3R1 alterations in NPC1 disease, we knocked-down or knocked-out PS1 in different cells and measured IP_3R1 distribution, activity, and G_qPCR-mediated Ca^{2+} release. First, using small interfering RNA (siRNA) directed against PS1 in eGFP-IP_3R1 HeLa cells, which decreases PS1 protein levels by 75% (20), we determined that IP_3R1 cluster areas were refractory to U18 treatment (Fig. 6 *A* and *B*). Second, aligned with its ability to normalize IP_3R1 clusters back to control sizes, PS1 knock-down in $NPC1^{I1061T}$ patient cells

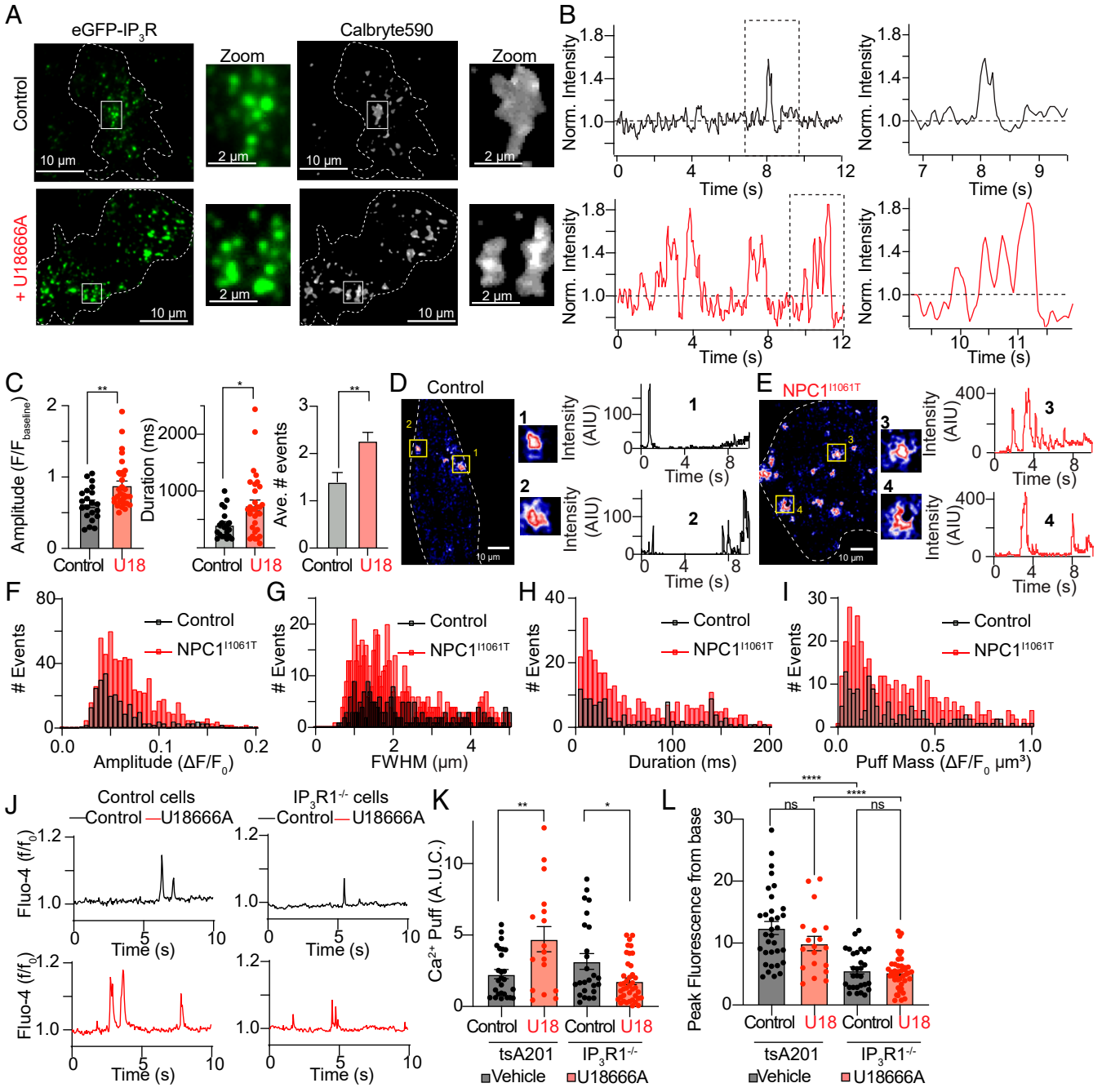

Fig. 4. Spontaneous intracellular IP_3R1 Ca^{2+} signaling is enhanced in NPC loss-of-function cells. (*A*) Representative maximum intensity projections of eGFP-IP_3R1 (*Left*) and Calbryte590 (*Right*) from control (*Top*) and U18-treated cells. Zoomed regions are taken from white rectangles. (*B*) Representative time series of spontaneous Ca^{2+} puffs in control cells (*Top*) and U18-treated (*Bottom*, red lines) cells. (*Right*) Zoomed time regions taken from dashed black rectangle. (*C*) Quantification of amplitude, duration, and number of spontaneous Ca^{2+} events. (*D*, *Left*) Representative maximum intensity projections from control fibroblasts loaded with Fluo-4. Zoomed regions are taken from solid yellow squares. (*Right*) Representative time series of spontaneous Ca^{2+} activity. (*E*) Same as *D*, only $NPC1^{I1061T}$ patient fibroblasts. (*F*) Frequency distribution of the amplitude of Ca^{2+} events from healthy fibroblasts (black) and $NPC1^{I1061T}$ disease fibroblasts (red). (*G*) Same as *F*, except showing the full-width half-max. (*H*) Same as *F*, except showing the duration of Ca^{2+} events. (*I*) Same as *F*, except showing Ca^{2+} puff mass. (*J*) Representative time series of Ca^{2+} events in control cells (*Left*) or $IP_3R1^{-/-}$ cells (*Right*) loaded with Fluo-4 and treated with either U18 (red) or vehicle control (black). (*K*) Quantitative analysis of Ca^{2+} puff area under the curve from the cell types and conditions in *J*. (*L*) Same as *K*, except analyzing Ca^{2+} puff peak fluorescence from base. All the data are expressed as mean ± SEM from individual cells. Statistical analyses were unpaired *t* tests except *K* and *L* which were two-way ANOVAs. ns: not significant; $*P < 0.05$; $**P < 0.01$; $****P < 0.0001$.

significantly reduced spontaneous $Ca^{2+}{}_{IP3R1}$ puffs back to control levels (Fig. 6*C*). Third, $NPC1^{I1061T}$ patient cells treated with siRNA PS1 had similar G_qPCR-mediated Ca^{2+} release as control (Fig. 6 *D* and *E*). As a final approach, we measured G_qPCR-mediated Ca^{2+} release from control ($PS1^{+/+}$) and PS1 knockout ($PS1^{-/-}$) mouse embryonic fibroblasts and determined that overnight U18 incubation increased G_qPCR Ca^{2+} release in $PS1^{+/+}$ cells (Fig. 6 *F* and *H*) but had no effect on $PS1^{-/-}$ cells relative to vehicle

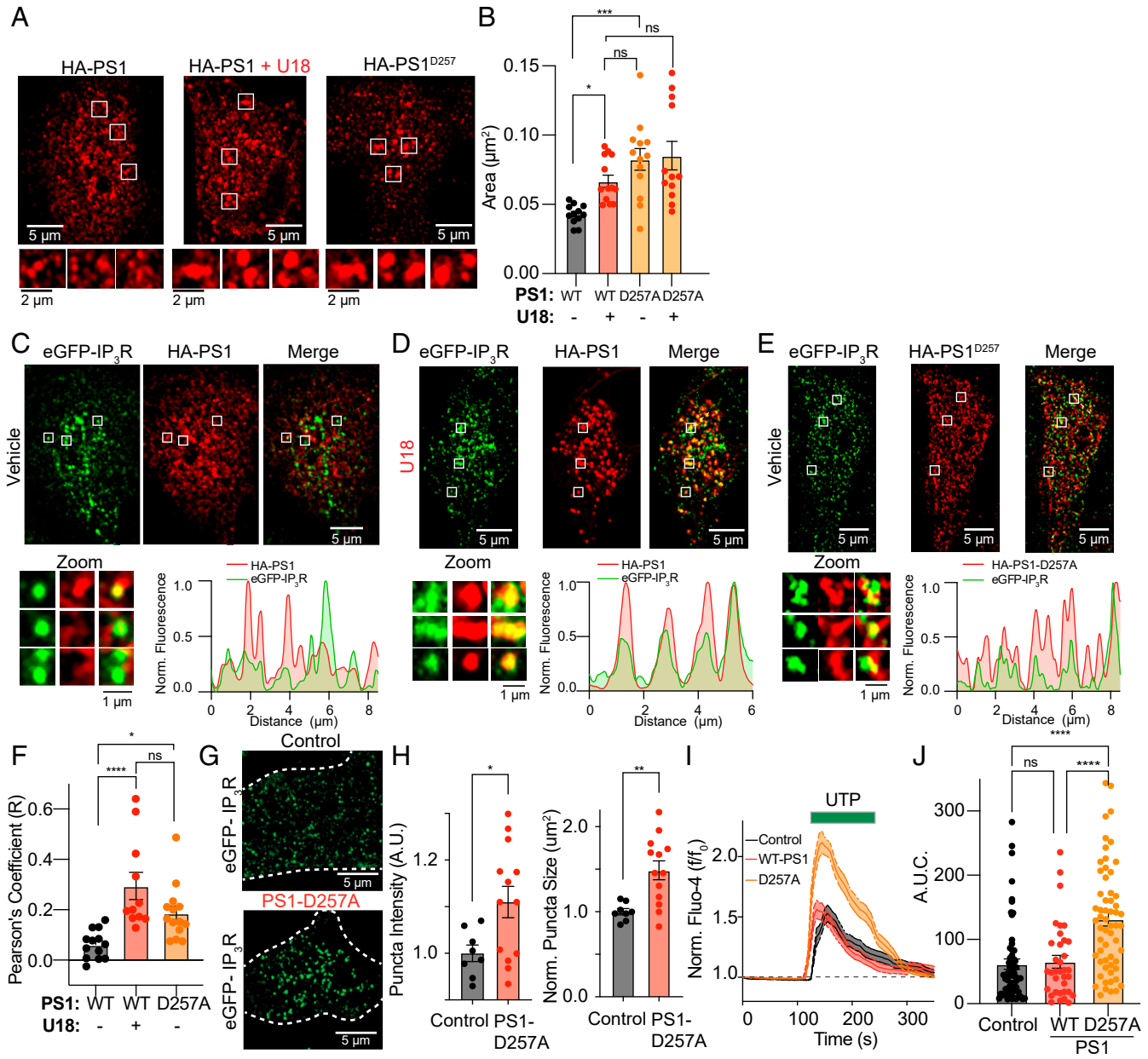

Fig. 5. Inhibition of NPC1 increases PS1 clusters and colocalization with IP_3R1. (*A*) Representative TIRF images of HeLa cells expressing HA-PS1, HA-PS1 + treated with U18, or HA-$PS1^{D257A}$. (*B*) Quantification of PS1 area normalized to footprint. (*C*, *Top*) TIRF images of eGFP-IP_3R HeLa cells transfected with HA-PS1-WT. (*Bottom*) Zoomed regions from solid white squares (*Left*) and line scan showing distribution of signals (*Right*). (*D*) Same as *C*, only treated with U18. (*E*) Same as *C*, only transfected with HA-$PS1^{D257A}$. (*F*) Quantitative analysis showing average Pearson's correlation coefficients from *C*–*E*. (*G*) Representative TIRF images from Control (*Top*) and HA-$PS1^{D257A}$-expressing eGFP-IP_3R HeLa cells. (*H*) Quantification of IP_3R1 puncta intensity and size in control and HA-$PS1^{D257A}$-expressing cells. (*I*) Average time series of Fluo-4 loaded control (black), HA-PS1-expressing (red), and HA-$PS1^{D257A}$-expressing (orange) tsA201 cells treated with UTP (100 µM). (*J*) Quantitative analysis of the UTP-evoked Ca^{2+} area under the curve. All the data are expressed as mean ± SEM from individual cells. Statistical analyses were unpaired *t* tests except (*B*) and (*F*) which were two-way and one-way ANOVAs, respectively. ns: not significant; $*P < 0.05$; $**P < 0.01$; $***P < 0.001$; $****P < 0.0001$.

controls (Fig. 6 *G* and *H*). Transfecting $PS1^{-/-}$ cells with PS1-WT reestablished U-18-mediated increases in G_qPCR Ca^{2+} release (*SI Appendix*, Fig. S7 *A* and *B*). Collectively, these data support the hypothesis that PS1-dependent increases in IP_3R1 cluster size drive puff activity and G_qPCR-mediated Ca^{2+} release in NPC1 disease.

Previously, we have reported that PS1 levels play a crucial role in decreasing ER Ca^{2+} ($Ca^{2+}{}_{ER}$) to drive synaptic remodeling of Purkinje neurons in the cerebellum (20). Given the published role that PS1 plays in enhancing the biophysical release properties of IP_3R1 (32, 31, 34) and the increases in spontaneous $Ca^{2+}{}_{IP3R1}$ puffs following loss of NPC1 function reported herein, we asked whether IP_3R1 is downstream of PS1 and involved in decreasing $Ca^{2+}{}_{ER}$ in NPC1 disease. To begin, we expressed a genetically encoded Ca^{2+} indicator targeted to the cytoplasmic leaflet of the ER membrane (Fig. 6*I*; ER-GCaMP3) in patient fibroblasts, U18-treated tsA cells, or $PS1^{D257A}$-expressing tsA cells to ask whether we could measure steady-state $Ca^{2+}{}_{ER}$ leak. Aligned with published data (20), both $NPC1^{I1061T}$ patient cells (Fig. 6*J*) and U18-treated tsA201 cells (Fig. 6*K*) exhibited significantly higher resting ER-GCaMP3 intensity values, consistent with increased $Ca^{2+}{}_{ER}$

leak following loss of NPC1 function. To probe a role for PS1–IP_3R1 interactions facilitating enhanced Ca^{2+}_{ER} leak in NPC1 disease, we performed similar experiments in $PS1^{-/-}$ and $IP_3R1^{-/-}$ cell lines and discovered that ER-GCaMP3 intensity values were refractory to U18 treatment under both conditions. These data suggest that PS1 and IP_3R1 are both key players in increasing Ca^{2+}_{ER} leak in NPC1 disease.

The consequence of increased Ca^{2+}_{ER} leak is a decrease in free Ca^{2+}_{ER} concentrations in NPC1 loss-of-function cells (20); thus, we tested the effect of knocking out IP_3R1 (Fig. 6*O*). We loaded $NPC1^{-/-}$ cells and $IP_3R1^{-/-}$ cells with the cytosolic Ca^{2+} dye, Fluo-4, and applied the SERCA inhibitor thapsigargin in a 0-mM, Ca^{2+}-containing extracellular solution. Treatment with thapsigargin gave the expected increase in cytoplasmic fluo-4 intensity from control cells, with $NPC1^{-/-}$ cells having a smaller increase in intensity (20) (Fig. 6 *P* and *Q*). Conducting similar experiments in $IP3R1^{-/-}$ cells treated with vehicle control or U18 did not result in any significantly differences in fluo-4 intensity following Thapsigargin treatment and provide evidence that increased PS1–IP_3R1 interactions drives decreased Ca^{2+}_{ER} in NPC1 disease (Fig. 6 *R* and *S*).

Inhibition of SREBP Prevents Increases in IP_3R1 Cluster Size and G_qPCR Ca^{2+} Following Loss of NPC1 Function. Loss of NPC1 function decreases lysosomal to ER cholesterol transport, resulting in depletion of ER membrane cholesterol and subsequent activation of the sterol regulatory element binding protein (SREBP) pathway, leading to increased gene expression of SREBP-dependent targets (35). We have previously reported that increased SREBP activity in NPC1 loss-of-function cells up-regulates expression of several Ca^{2+}-handling proteins, including PS1, with inhibition of the SREBP pathway reversing differential protein expression along with aberrant ER Ca^{2+} and SOCE phenotypes (20). Thus, we wanted to determine whether the SREBP pathway is involved in the remodeling of IP_3Rs and potentiated G_qPCR-mediated Ca^{2+} release. To begin, we conducted qPCR experiments on $NPC1^{I1061T}$ cells to determine whether mRNA levels of each IP_3R isoform are altered. Consistent with Western blot data, mRNA levels for IP_3R1, but not IP_3R2 or IP_3R3, were increased in $NPC1^{I1061T}$ cells (Fig. 7*A*). Treating cells overnight with the SREBP inhibitor, PF-429242 (500 nM), abolished increases in IP_3R1 levels from $NPC1^{I1061T}$ cells without affecting steady-state mRNA levels of IP_3R2 or IP_3R3. Furnished with the information that PF-429242 can decrease IP_3R1 mRNA levels, we next asked whether PF-429242 treatment rescues IP_3R1 cluster size in NPC1 loss-of-function cells. To answer this question, we treated eGFP-IP_3R1 cells with U18, or U18 and PF-429242, before quantifying IP_3R1 clusters using TIRF microscopy (Fig. 7*B*). Similar to the observed decreases in mRNA levels, treatment with PF-429242 decreased IP_3R1 cluster size back to control levels (Fig. 7*C*). Next, we measured G_qPCR-mediated Ca^{2+} release to test whether PF-429242-mediated decreases in IP_3R1 mRNA and cluster size would also decrease Ca^{2+} release. Analysis of intracellular Fluo-4 intensity following application of histamine determined that PF-429242 reduces the G_qPCR evoked Ca^{2+} signal in NPC1 fibroblasts back to healthy fibroblast control levels. Finally, we conducted G_qPCR experiments in $SCAP^{-/-}$ cells that lack a functional SREBP pathway (36) and found that U18 treatment resulted in a slight decrease in Ca^{2+} release following receptor activation (Fig. 7 *F* and *G*). Therefore, like other Ca^{2+}-handling proteins that are increased in NPC1 disease, IP_3R1 can be normalized back to control levels following inhibition of SREBP.

IP_3R1 Drives Ca^{2+}-Dependent NFAT Translocation and Cytotoxic Elevations in Mitochondrial Ca^{2+} Following Loss of NPC1 Function. Finally, we wanted to begin elucidating the cellular consequences of aberrant nanoscale distribution and activity of the IP_3R in NPC1 disease. Because alterations in cytoplasmic Ca^{2+} and IP_3R-mediated Ca^{2+} release are fundamentally required for many cellular processes, we focused on two of these pathways: NFAT signaling (37) and mitochondrial Ca^{2+} (13) (Ca^{2+}_{Mito}) to ask whether they are altered in NPC1 disease.

NFAT proteins are a family of transcription factors who are phosphorylated and reside in the cytoplasm. Upon IP_3R stimulation to simultaneously elevate intracellular Ca^{2+} concentrations and deplete Ca^{2+}_{ER}, thereby activating store-operated Ca^{2+} entry, NFATs are dephosphorylated by the Ca^{2+}/calmodulin-dependent serine phosphatase, calcineurin, and translocate to the nucleus to become active (Fig. 8*A*). First, we tested whether steady-state NFAT distribution is different between control and $NPC1^{I1061T}$ cells; analysis of fluorescence intensity ratios between the cytoplasm and nucleus revealed that $NPC1^{I1061T}$ cells had a small but significant increase in the proportion of NFAT in the nucleus (Fig. 8 *B* and *C*). A similar distribution was observed in U18-treated cells (Fig. 8*D*). To test whether IP_3R1 is involved in mediating steady-state increases in nuclear NFAT in NPC1 loss-of-function cells, we performed similar experiments in $IP_3R1^{-/-}$ cells. Quantification of NFAT cytoplasmic/nuclear intensities from U18-treated $IP_3R1^{-/-}$ disclosed that NFAT no longer preferentially accumulated in the nucleus at steady-state (Fig. 8*D*). Next, we tested whether G_qPCR-stimulated NFAT translocation was also different between control and $NPC1^{I1061T}$ patient cells. Time series analysis revealed that 100-s histamine application, a stimulus that increases cytoplasmic Ca^{2+} (Fig. 1*F*), increased NFAT more quickly in the nucleus of $NPC1^{I1061T}$ cells relative to control (Fig. 8*E*). Thus, there is a correlation between the amount of G_qPCR-Ca^{2+} release and NFAT translocation. To probe the involvement of IP_3R1, we repeated experiments in tsA201 cells and $IP_3R1^{-/-}$ cells treated with U18. Similar to $NPC1^{I1061T}$ patient cells, treatment of tsA201 cells with U18 significantly increased NFAT translocation to the nucleus (Fig. 8*F*), an increase that was completely absent in $IP_3R1^{-/-}$ cells (Fig. 8*G*). These experiments provide evidence that NPC1-dependent increases in IP_3R1 increase NFAT signaling in NPC1 disease.

As a final test to determine the cellular consequences of altered IP_3R1 signaling in NPC1 disease, we investigated Ca^{2+}_{Mito} and cell viability. Ca^{2+} represents a key rheostat that couples mitochondria biogenetics to cellular demand and is frequently altered in pathophysiological conditions, including neurodegeneration. Intimate interactions between VDAC1 on mitochondria membranes and IP_3R1 on ER membranes provide the platform for constitutive IP_3R-mediated Ca^{2+} release to maintain cellular bioenergetics to meet cellular demands (38) (Fig. 8*H*). Given the importance of IP_3R1 in regulating Ca^{2+}_{Mito}, we expressed a genetically encoded Ca^{2+} indicator targeted to mitochondria (Mito-RCaMPh1) to ask whether Ca^{2+}_{Mito} is altered following loss of NPC1 function. Quantification of Mito-RCaMPh1 intensities between cells treated with a vehicle or U18 rvealed that loss of NPC1 function significantly increased Ca^{2+}_{Mito} (Fig. 8 *I* and *J*). Identical experiments conducted on $IP_3R1^{-/-}$ cells revealed reduced Ca^{2+}_{Mito} levels compared to control with $IP_3R1^{-/-}$ cells now being refractory to U18 treatment (Fig. 8*J*). In parallel, we asked whether increases in Ca^{2+}_{Mito}, which can be cytotoxic in neurodegenerative conditions, are accompanied by changes in cell health. Consistent with this hypothesis, cell viability assays determined U18-dependent increases in Ca^{2+}_{Mito} correlated with increased cell death (Fig. 8*K*), an observation that was completely absent in $IP_3R1^{-/-}$ cells. Collectively, these data suggest that NPC1-dependent increases in IP_3R1 distribution/activity increase Ca^{2+}_{Mito} cytotoxicity in NPC1 disease and presents the IP_3R as a potential target to slow neurodegeneration.

Discussion

Dysfunction of IP_3Rs is a common feature across many neurodegenerative diseases (39–41); thus, determining molecular details regarding their regulation and control is imperative for

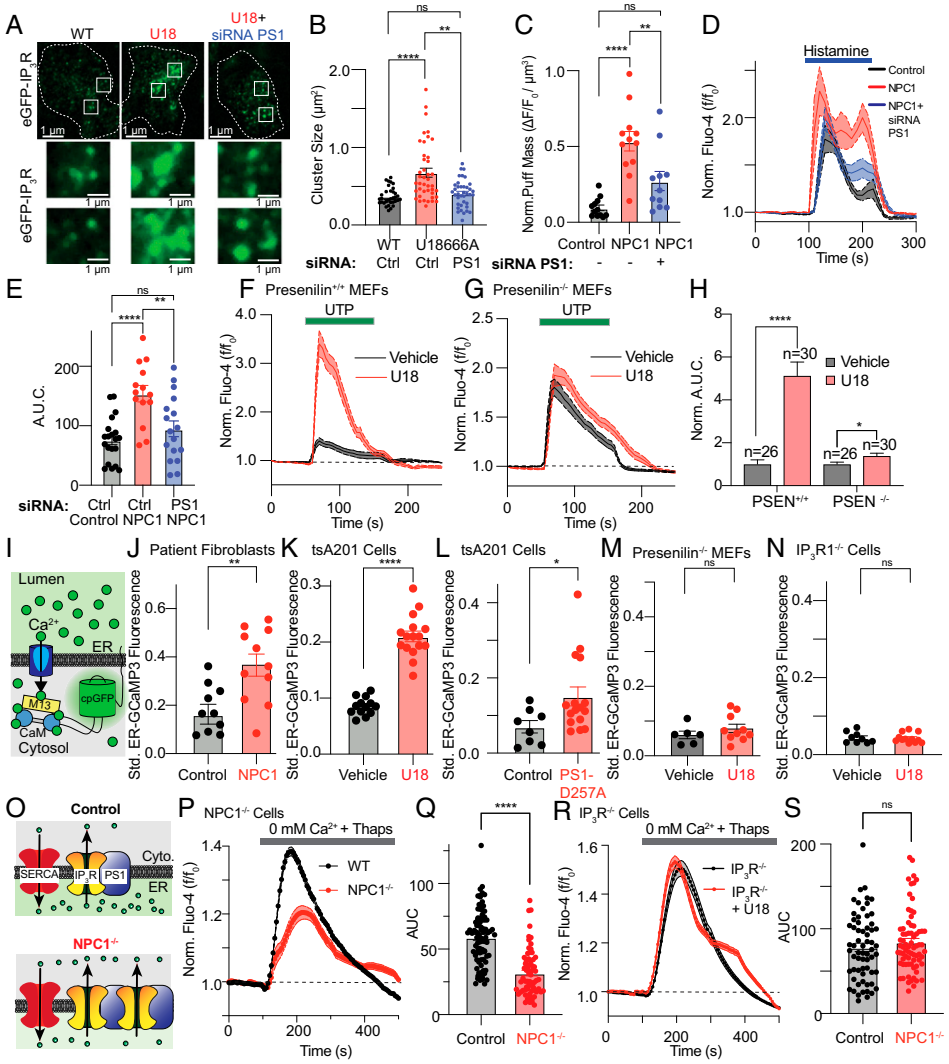

Fig. 6. Knocking out PS1 or IP_3R1 rescues Ca^{2+} defects in NPC1 disease cells. (*A*) Representative TIRF images from control, U18-treated, and U18-treated + siRNA PS1 eGFP-IP_3R1 cells. Zoomed areas are taken from the solid white squares. (*B*) Quantification of eGFP-IP_3R1 cluster size. (*C*) Quantification of spontaneous Ca^{2+} activity. (*D*) Average time series of histamine responses from Fluo-4 loaded control (black), $NPC1^{I1061T}$(red), and $NPC1^{I1061T}$ + siRNA PS1 (blue) fibroblasts. (*E*) Quantitative analysis of the histamine-evoked Ca^{2+} area under the curve (A.U.C). (*F*) Average time series of UTP responses from Fluo-4 loaded $PSEN^{+/+}$ MEF cells treated with vehicle control (black) or U18 (red). (*G*) Same as *F*, only $PS1^{-/-}$ cells. (*H*) Quantification of UTP-evoked Fluo-4 signals. (*I*) Schematic of genetically encoded ER-GCaMP3 Ca^{2+} indicator. (*J*) Quantification of normalized ER-GCaMP3 intensity in patient fibroblasts. (*K*) Same as *L*, only tsA201 cells treated with U18. (*L*) Same as *K*, only tsA201 cells expressing $PS1^{D257A}$. (*M*) Same as *K*, only $PS1^{-/-}$ cells. (*N*) Same as *K*, only $IP_3R1^{-/-}$ cells. (*O*) Schematic of IP_3R1–PS1 hypothesis in NPC1 disease. (*P*) Average time series of thapsigargin responses from Fluo-4 loaded control (black line) and $NPC1^{-/-}$ (red line) cells. (*Q*) Quantification of area under thapsigargin responses. (*R*) Same as *P*, except $IP_3R1^{-/-}$ cells. (*S*) Same as *Q*. All the data are expressed as mean ± SEM from individual cells. *B*, *C*, and *E* were one-way ANOVAs; *H* was a two-way ANOVA; and *J*–*N*, *Q*, and *S* were unpaired *t* tests. ns: not significant; $*P < 0.05$; $**P < 0.01$; $****P < 0.0001$.

human health. Here, we discover a signaling axis that links the NPC1 lysosomal cholesterol transporter to the nanoscale distribution and activity of IP_3R1 (*SI Appendix*, Fig. S8). We show that loss of NPC1 function results in augmented clustering of IP_3R1 near the PM, increased frequency and size of spontaneous Ca^{2+} puffs from IP_3Rs, and enhanced G_qPCR-mediated intracellular Ca^{2+} signaling. Upstream of changes in IP_3R1 appears to be PS1, with overexpression of $PS1^{D257A}$ phenocopying the observed changes in NPC1 disease cells. Mechanistically linking cholesterol egress from the lysosome to IP_3R1-dependent alterations in Ca^{2+} is the SREBP pathway, with inhibition of this transcription pathway restoring mRNA levels, IP_3R1 cluster size, and G_qPCR signaling, respectively. Functionally, altered IP_3R1 distribution/activity leads to increased steady-state and stimulated Ca^{2+}-dependent NFAT signaling and $Ca^{2+}{}_{mito}$ toxicity.

G_qPCRs are pivotal purveyors of physiological information, transducing fluctuations in hormones, growth factors, and neurotransmitters across the PM to stimulate intracellular second messengers that initiate downstream signaling cascades. In this study, we determine that the PM-localized elements of G_qPCR signaling cascades, namely receptor, G_q, and PLC, are unaltered or, in the case of $PI(4,5)P_2$, decreased (19) following loss of NPC1 function. These observations, coupled with decreased $Ca^{2+}{}_{ER}$ levels (20), made it surprising to find that both receptor-activated and spontaneous IP_3R1-mediated Ca^{2+} responses are amplified in NPC1 disease cells. This counterintuitive discovery can be reconciled with information that IP_3R1 protein abundance, nanoscale distribution, mobility near the PM, and activity are all enhanced in NPC1 disease. The degree of spatial, temporal, and allosteric plasticity exhibited by IP_3R1 has been previously reported

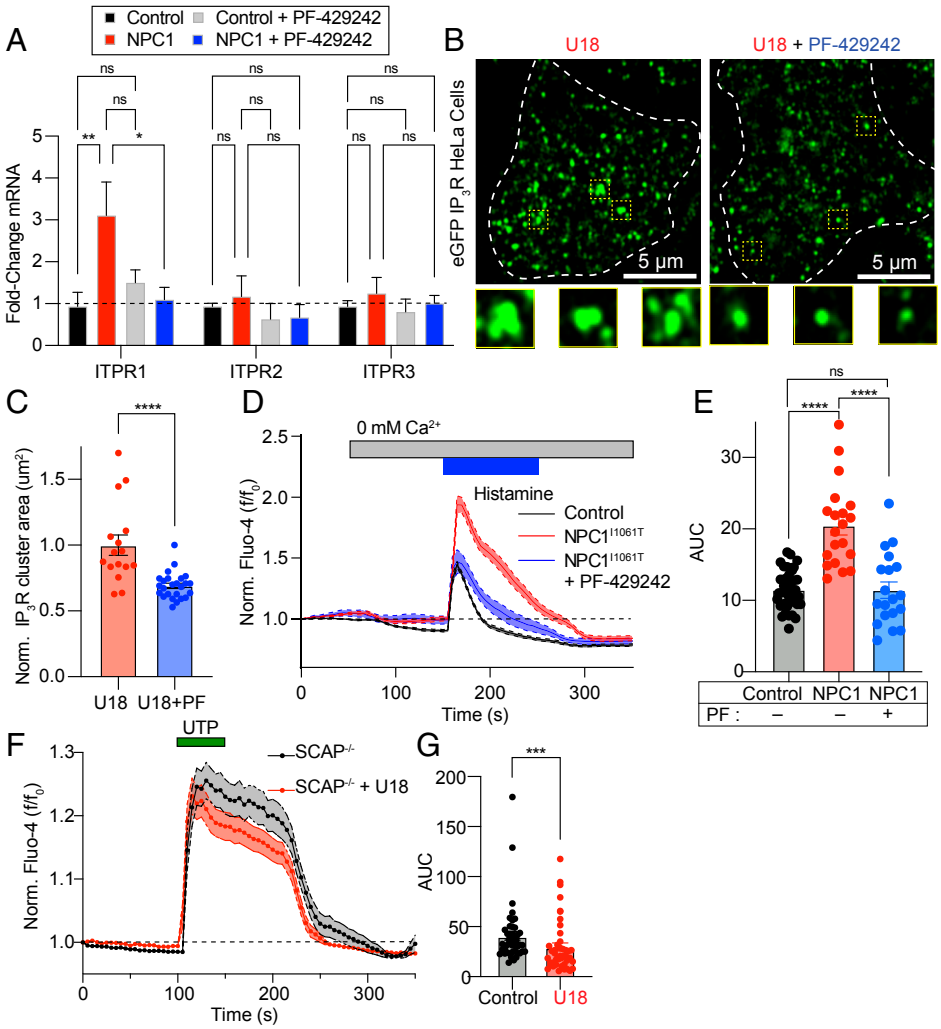

Fig. 7. Inhibition or loss of SREBP pathway activity rescues expression and distribution of IP_3R1 and Ca^{2+} phenotypes in NPC1 disease. (*A*) Quantification of ITPR1, ITPR2, and ITPR3 mRNA levels in control (black), control + PF-429242 (gray), $NPC1^{I1061T}$ (red), and $NPC1^{I1061T}$ + PF-429242 (blue) patient fibroblasts. (*B*) Representative TIRF images form eGFP-IP_3R1 HeLa cells treated with U18 (*Left*) or U18 and PF-429242. (*C*) Quantification of IP_3R1 cluster size. (*D*) Average time series of histamine responses from Fluo-4 loaded control (black line), $NPC1^{I1061T}$ (red line) cells, and $NPC1^{I1061T}$ + PF429242 fibroblasts. (*E*) Quantification of area under the histamine responses. (*F*) Average time series of UTP responses from Fluo-4 loaded control (black line) or U18-treated (red line) $SCAP^{-/-}$ cells. (*G*) Quantification of area under the UTP responses. All the data are expressed as mean ± SEM from individual cells. Statistical significance was calculated using the following test: *A*, two-way ANOVA; *C* and *G*, unpaired *t* tests; and *E*, one-way ANOVA. ns: not significant; $*P < 0.05$; $**P < 0.01$; $***P < 0.001$; $****P < 0.0001$.

(25, 31, 42); we add another modulatory mechanism for IP_3R1 and G_qPCR-mediated Ca^{2+} release through NPC1 abundance and/or cholesterol egress across lysosomal–ER MCS. This positions NPC1 and lysosomal–ER MCS as potential targets to tune G_qPCR signaling with the goal of altering global or local Ca^{2+} release to modify neuronal bioenergetics, Ca^{2+}-dependent transcription, or synaptic plasticity in health or disease.

We detail an important role for PS1 in regulating IP_3R1 distribution and activity following loss of NPC1 function. Under normal physiological conditions, PS1 undergoes autoproteolytic cleavage, resulting in two fragments (N and C terminals) that associate with other proteins to create the γ-secretase complex. Several mutations in the gene encoding PS1 can abolish this autoproteolytic activity, keeping PS1 in an uncleaved and full-length state, which is purported to form Ca^{2+} leak channels at the ER membrane (33). Contrasting the hypothesis that PS1 is a Ca^{2+} leak channel, Cheung et al. have reported that both Familial Alzheimer's Disease–linked PS1 mutations, which lack the ER Ca^{2+} leak activity, as well as the catalytically dead PS1 mutants that maintain their full uncleaved length bind and enhance the gating properties of IP_3Rs (31), suggesting the mechanism of $Ca^{2+}{}_{ER}$ leak involves physical interactions between PS1 and IP_3R1. We find that PS1 and IP_3Rs have little colocalization after overexpression of wild-type PS1; however, inhibition of NPC1 significantly increased their localization with one another. Additionally, overexpression of the catalytically dead $PS1^{D257A}$ mutation that results in increased full-length protein form reorganizes IP_3R1 nanoscale distribution, spontaneous puff activity, and G_qPCR-mediated Ca^{2+} release, independent of NPC1 inhibition. Finally, $IP_3R1^{-/-}$ cells are refractory to U18 with no NPC1-dependent Ca^{2+} phenotypes. This leads us to suggest that it is the physical interactions between PS1 and IP_3R1, coupled with elevations in cytoplasmic Ca^{2+} (20), that modify the clustering properties of IP_3R1 to enhance their cooperative gating and thereby their release probability in NPC disease. If this model is correct, it would position IP_3R1-mediated Ca^{2+} release as the distal element underlying enhanced $Ca^{2+}{}_{ER}$ leak in NPC1 disease. Questions remain to fully determine the molecular choreography of PS1–IP_3R1 complex, including the following: 1) What is the optimal stoichiometry of PS1–IP_3R1 interactions? 2) Do decreases in IP_3R1 mobility act as a diffusion trap for PS1 to bind,

aggregate, and influence IP_3R1? 3) Does decreased ER cholesterol in NPC1 cells, as evidenced by enhanced SREBP processing (20), reduce cholesterol-dependent partitioning of PS1 and IP_3R1 to allow their increased clustering/interaction? and 4) Are there other accessory proteins that exert regulatory influence over this signaling complex?

The SREBP transcription factor appears to link changes in NPC1 function to alterations in IP_3R1 and G_qPCR signaling. Previously, we have reported that the SREBP pathway is involved in mediating expressional changes in the Ca^{2+}-handling proteins SERCA, STIM1, ORAI1, and PS1 in $NPC1^{I1061T}$ cells; therefore, it is perhaps not surprising that the IP_3R1 is also influenced by SREBP. That being said, it is still unknown whether regulation of IP_3R1 by SREBP is through direct or indirect transcriptional regulation. Further, a key question that remains unanswered is whether alterations in intracellular Ca^{2+} signaling are purely deleterious sequences (see paragraph below) or are part of a molecular mechanism(s) attempting to correct the cellular phenotypes of NPC1 disease. There are clear links between elevations in intracellular Ca^{2+} levels and endocytic fusion and transport events; further, decreasing $Ca^{2+}{}_{ER}$ has been reported to redistribute the intracellular pool of unesterified cholesterol (43) and rescue key cellular phenotypes of NPC1 disease (6), while knocking out INPP5A (44) (IP_3 5-phosphatase) triggers depletion of cellular cholesterol. Thus, changes in $Ca^{2+}{}_{ER}$ signaling may be a key rheostat for maintenance and control of cellular cholesterol homeostasis.

Ca^{2+}-handling proteins have been linked to a host of pathologies, including several neurodegenerative disorders (33, 34). MCS between the ER and mitochondrial are regions of intimate membrane apposition that facilitate transport of Ca^{2+} from the ER to the mitochondria. Following G_qPCR activation or spontaneous IP_3R opening, Ca^{2+} is taken up into mitochondria to participate in the control of bioenergetics by activating oxidative metabolism, mitochondrial respiration, and ATP synthesis. Notably, dysregulation of $Ca^{2+}{}_{Mito}$ are potent triggers of necrosis, apoptosis, and autophagy (for review, refer to ref. 45). Here, we present evidence that NPC1-dependent increases in IP_3R1 distribution and activity increase $Ca^{2+}{}_{Mito}$ to enhance cell death in NPC1 disease models. Thus, although increased Ca^{2+} release from the ER may be initiated as a mechanism to alter cholesterol homeostasis or redistribute toxic metabolites associated with NPC1 disease mutations, the prolonged elevations in cytoplasmic and $Ca^{2+}{}_{Mito}$ could ultimately be a central driver of neuronal cell death in NPC disease. This presents IP_3R1 and MAMs as potential therapeutic targets to correct Ca^{2+} phenotypes in order to slow Purkinje neuron neurodegeneration and NPC disease progression.

In conclusion, we characterize a link between the lysosomal NPC1 cholesterol transporter and changes in IP_3R-dependent Ca^{2+} signaling. We find that differential expressional and localization of IP_3R1 enhances both spontaneous and G_qPCR-mediated Ca^{2+} release to promote mitochondrial cytotoxicity. This work furthers our understanding of the regulatory factors that tune IP_3R

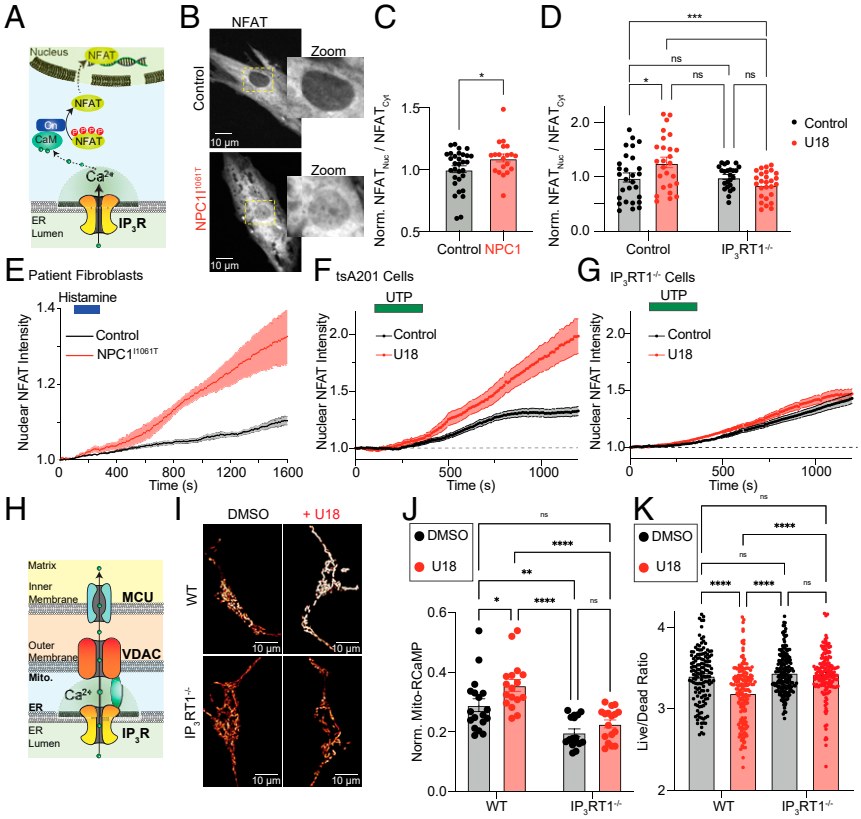

Fig. 8. Knockout of IP_3R1 rescues Ca^{2+}-dependent gene transcription and $Ca^{2+}{}_{Mito}$ cytotoxicity in NPC1 loss-of-function cells. (*A*) Schematic of NFAT translocation to the nucleus. (*B*) Representative images from control (*Top*) and $NPC1^{I1061T}$ (*Bottom*) fibroblasts expressing NFAT. (*C*) Quantification of NFAT intensity in the nucleus relative to the cytoplasm in control and $NPC1^{I1061T}$ fibroblasts. (*D*) Same analysis as *C*, only using control and $IP_3R1^{-/-}$ cells. (*E*) Averaged time series of nuclear NFAT intensity following the addition of Histamine in control (black line) and $NPC1^{I1061T}$ (red line) fibroblasts. (*F*) Same as *E*, only UTP application in control and U18-treated tsA201 cells. (*G*) Same as *F*, only using $IP_3R1^{-/-}$ cells. (*H*) Schematic of Ca^{2+} transfer at ER–mitochondria MCS. (*I*) Representative images of Mito-RCaMP in control (*Top*) and $IP_3R1^{-/-}$ cells (*Bottom*) treated with vehicle control (*Left*) or U18 (*Right*). (*J*) Quantification of normalized Mito-RCaMP intensity in control and $IP_3R1^{-/-}$ cells. (*K*) Quantification of live cell/dead cell ratio in control and $IP_3R1^{-/-}$ cells treated with vehicle control or U18. All the data are expressed as mean ± SEM from individual cells. Statistical significance was calculated using the following tests: *C*, unpaired *t* test and *D*, *J*, and *K*, two-way ANOVA. ns: not significant; $*P < 0.05$; $**P < 0.01$; $****P < 0.0001$.

signaling, most importantly PS1, whose form and expression are altered in NPC1 disease. By elucidating these regulatory pathways, we have provided potential therapeutic targets to address IP_3R dysfunction, a feature of NPC1 disease and other neurodegenerative disorders.

Materials and Methods

Detailed methods can be found in *SI Appendix*. Briefly, $NPC1^{I1061T}$ patient cells, $NPC1^{-/-}$ cells, and tsA201 cells treated overnight with U18666A and male and female $NPC1^{I1061T}$ mice served as models of NPC disease and were comparted to control cells in this study. Protein levels were determined using immunoblot approaches. Ca^{2+} imaging was performed using an Andor W1 spinning disk system. Immunofluorescence TIRF, superresolution, and confocal images were acquired using a Leica single-molecule localization system or a Zeiss AiryScan confocal microscope.

Data Availability. All study data are included in the article and/or *SI Appendix*.

ACKNOWLEDGMENTS. We are extremely grateful to those laboratories that shared reagents, plasmids, and cells lines used in this study. We thank Dr. Oscar Vivas for technical assistance. This work was supported by an Ara Parseghian Medical Research Foundation award (E.J.D.); University of California funds (E.J.D.); NIH grant R01 GM127513 (E.J.D.); NIH T32 training award T32GM099608 (S.A.T.); and NIH grants R01 NS114210 and HL144071 (L.F.S.), R01 NS109176 (S.S.), R01 HL06773 (D.S.O.), and R01 AG063796 (R.E.D.).

1. A. Ghosh, M. E. Greenberg, Calcium signaling in neurons: Molecular mechanisms and cellular consequences. *Science* **268**, 239–247 (1995).
2. I. Bezprozvanny, Calcium signaling and neurodegenerative diseases. *Trends Mol. Med.* **15**, 89–100 (2009).
3. J. K. Foskett, C. White, K.-H. Cheung, D.-O. D. Mak, Inositol trisphosphate receptor Ca2+ release channels. *Physiol. Rev.* **87**, 593–658 (2007).
4. D. L. Prole, C. W. Taylor, Structure and function of IP_3 receptors. *Cold Spring Harb. Perspect. Biol.* **11**, 11–17 (2019).
5. S. A. Tiscione *et al*., Disease-associated mutations in Niemann-Pick type C1 alter ER calcium signaling and neuronal plasticity. *J. Cell Biol.* **218**, 4141–4156 (2019).
6. E. Lloyd-Evans *et al*., Niemann-Pick disease type C1 is a sphingosine storage disease that causes deregulation of lysosomal calcium. *Nat. Med.* **14**, 1247–1255 (2008).
7. D. Shen *et al*., Lipid storage disorders block lysosomal trafficking by inhibiting a TRP channel and lysosomal calcium release. *Nat. Commun.* **3**, 731 (2012).
8. M. J. Berridge, Calcium hypothesis of Alzheimer's disease. *Pflugers Arch.* **459**, 441–449 (2010).
9. T. Furuichi *et al*., Widespread expression of inositol 1,4,5-trisphosphate receptor type 1 gene (Insp3r1) in the mouse central nervous system. *Receptors Channels* **1**, 11–24 (1993).
10. J. R. Sarna *et al*., Patterned Purkinje cell degeneration in mouse models of Niemann-Pick type C disease. *J. Comp. Neurol.* **456**, 279–291 (2003).
11. M. J. Berridge, The inositol trisphosphate/calcium signaling pathway in health and disease. *Physiol. Rev.* **96**, 1261–1296 (2016).
12. T. Inoue, K. Kato, K. Kohda, K. Mikoshiba, Type 1 inositol 1,4,5-trisphosphate receptor is required for induction of long-term depression in cerebellar Purkinje neurons. *J. Neurosci.* **18**, 5366–5373 (1998).
13. R. Rizzuto *et al*., Close contacts with the endoplasmic reticulum as determinants of mitochondrial Ca2+ responses. *Science* **280**, 1763–1766 (1998).
14. M. Matsumoto *et al*., Ataxia and epileptic seizures in mice lacking type 1 inositol 1,4,5-trisphosphate receptor. *Nature* **379**, 168–171 (1996).
15. C. Hisatsune *et al*., IP3R1 deficiency in the cerebellum/brainstem causes basal ganglia-independent dystonia by triggering tonic Purkinje cell firings in mice. *Front. Neural Circuits* **7**, 156 (2013).
16. J. van de Leemput *et al*., Sequencing analysis of the ITPR1 gene in a pure autosomal dominant spinocerebellar ataxia series. *Mov. Disord.* **25**, 771–773 (2010).
17. S. Barresi *et al*., Mutations in the IRBIT domain of ITPR1 are a frequent cause of autosomal dominant nonprogressive congenital ataxia. *Clin. Genet.* **91**, 86–91 (2017).
18. S. Gerber *et al*., Recessive and dominant de novo ITPR1 mutations cause Gillespie syndrome. *Am. J. Hum. Genet.* **98**, 971–980 (2016).
19. O. Vivas, S. A. Tiscione, R. E. Dixon, D. S. Ory, E. J. Dickson, Niemann-Pick type C disease reveals a link between lysosomal cholesterol and $PtdIns(4,5)P_2$ that regulates neuronal excitability. *Cell Rep.* **27**, 2636–2648.e4 (2019).
20. S. A. Tiscione *et al*., Disease-associated mutations in Niemann-Pick type C1 alter ER calcium signaling and neuronal plasticity. *J. Cell Biol.* **218**, 4141–4156 (2019).
21. F. Lu *et al*., Identification of NPC1 as the target of U18666A, an inhibitor of lysosomal cholesterol export and Ebola infection. *eLife* **4**, e12177 (2015).
22. M. Praggastis *et al*., A murine Niemann-Pick C1 I1061T knock-in model recapitulates the pathological features of the most prevalent human disease allele. *J. Neurosci.* **35**, 8091–8106 (2015).
23. Y. Higashi, S. Murayama, P. G. Pentchev, K. Suzuki, Cerebellar degeneration in the Niemann-Pick type C mouse. *Acta Neuropathol.* **85**, 175–184 (1993).
24. E. J. Dickson, B. H. Falkenburger, B. Hille, Quantitative properties and receptor reserve of the $IP(_3)$ and calcium branch of $G(_q)$-coupled receptor signaling. *J. Gen. Physiol.* **141**, 521–535 (2013).
25. Taufiq-Ur-Rahman, A. Skupin, M. Falcke, C. W. Taylor, Clustering of InsP3 receptors by InsP3 retunes their regulation by InsP3 and Ca2+. *Nature* **458**, 655–659 (2009).
26. C. W. Taylor, S. C. Tovey, IP(3) receptors: toward understanding their activation. *Cold Spring Harb. Perspect. Biol.* **2**, a004010 (2010).
27. T. Rahman, C. W. Taylor, Nuclear patch-clamp recording from inositol 1,4,5-trisphosphate receptors. *Methods Cell Biol.* **99**, 199–224 (2010).
28. N. B. Thillaiappan, A. P. Chavda, S. C. Tovey, D. L. Prole, C. W. Taylor, Ca^{2+} signals initiate at immobile IP_3 receptors adjacent to ER-plasma membrane junctions. *Nat. Commun.* **8**, 1505 (2017).
29. E. J. Dickson *et al*., Dynamic formation of ER-PM junctions presents a lipid phosphatase to regulate phosphoinositides. *J. Cell Biol.* **213**, 33–48 (2016).
30. G. D. Dickinson, D. Swaminathan, I. Parker, The probability of triggering calcium puffs is linearly related to the number of inositol trisphosphate receptors in a cluster. *Biophys. J.* **102**, 1826–1836 (2012).
31. K. H. Cheung *et al*., Mechanism of Ca2+ disruption in Alzheimer's disease by presenilin regulation of InsP3 receptor channel gating. *Neuron* **58**, 871–883 (2008).
32. D. Shilling *et al*., Suppression of $InsP_3$ receptor-mediated Ca^{2+} signaling alleviates mutant presenilin-linked familial Alzheimer's disease pathogenesis. *J. Neurosci.* **34**, 6910–6923 (2014).
33. H. Tu *et al*., Presenilins form ER Ca^{2+} leak channels, a function disrupted by familial Alzheimer's disease-linked mutations. *Cell* **126**, 981–993 (2006).
34. G. E. Stutzmann, A. Caccamo, F. M. LaFerla, I. Parker, Dysregulated IP3 signaling in cortical neurons of knock-in mice expressing an Alzheimer's-linked mutation in presenilin1 results in exaggerated Ca2+ signals and altered membrane excitability. *J. Neurosci.* **24**, 508–513 (2004).
35. M. S. Brown, J. L. Goldstein, The SREBP pathway: Regulation of cholesterol metabolism by proteolysis of a membrane-bound transcription factor. *Cell* **89**, 331–340 (1997).
36. R. B. Rawson, R. DeBose-Boyd, J. L. Goldstein, M. S. Brown, Failure to cleave sterol regulatory element-binding proteins (SREBPs) causes cholesterol auxotrophy in Chinese hamster ovary cells with genetic absence of SREBP cleavage-activating protein. *J. Biol. Chem.* **274**, 28549–28556 (1999).
37. M. F. Gomez, A. S. Stevenson, A. D. Bonev, D. C. Hill-Eubanks, M. T. Nelson, Opposing actions of inositol 1,4,5-trisphosphate and ryanodine receptors on nuclear factor of activated T-cells regulation in smooth muscle. *J. Biol. Chem.* **277**, 37756–37764 (2002).
38. C. Cárdenas *et al*., Essential regulation of cell bioenergetics by constitutive InsP3 receptor Ca2+ transfer to mitochondria. *Cell* **142**, 270–283 (2010).
39. C. Hisatsune, K. Mikoshiba, IP_3 receptor mutations and brain diseases in human and rodents. *J. Neurochem.* **141**, 790–807 (2017).
40. P. Egorova, E. Popugaeva, I. Bezprozvanny, Disturbed calcium signaling in spinocerebellar ataxias and Alzheimer's disease. *Semin. Cell Dev. Biol.* **40**, 127–133 (2015).
41. I. Bezprozvanny, Role of inositol 1,4,5-trisphosphate receptors in pathogenesis of Huntington's disease and spinocerebellar ataxias. *Neurochem. Res.* **36**, 1186–1197 (2011).
42. J. Shuai, H. J. Rose, I. Parker, The number and spatial distribution of IP3 receptors underlying calcium puffs in Xenopus oocytes. *Biophys. J.* **91**, 4033–4044 (2006).
43. W. A. Wang *et al*., Loss of calreticulin uncovers a critical role for calcium in regulating cellular lipid homeostasis. *Sci. Rep.* **7**, 5941 (2017).
44. M. Malek *et al*., Inositol triphosphate-triggered calcium release blocks lipid exchange at endoplasmic reticulum-Golgi contact sites. *Nat. Commun.* **12**, 2673 (2021).
45. C. Giorgi, S. Marchi, P. Pinton, The machineries, regulation and cellular functions of mitochondrial calcium. *Nat. Rev. Mol. Cell Biol.* **19**, 713–730 (2018).